Supporting Information

Adenovirus Mimetic Nanoparticles: Sequential Ligand-Receptor Interplay as a Universal Tool for Enhanced *In Vitro/In Vivo* Cell Identification

*Daniel Fleischmann, Sara Maslanka Figueroa, Sebastian Beck, Kathrin Abstiens, Ralph Witzgall, Frank Schweda, Philipp Tauber, Achim Goepferich**

D. Fleischmann, S. Maslanka Figueroa, S. Beck, Dr. K. Abstiens, Prof. A. Goepferich
Department of Pharmaceutical Technology, University of Regensburg, Universitaetsstrasse 31, 93053 Regensburg, Germany
E-mail: Achim.Goepferich@ur.de

Prof. R. Witzgall
Institute for Molecular and Cellular Anatomy, University of Regensburg, 93053 Regensburg, Germany

Dr. P. Tauber, Prof. F. Schweda
Department of Physiology II, Institute for Physiology, University of Regensburg, 93053 Regensburg, Germany

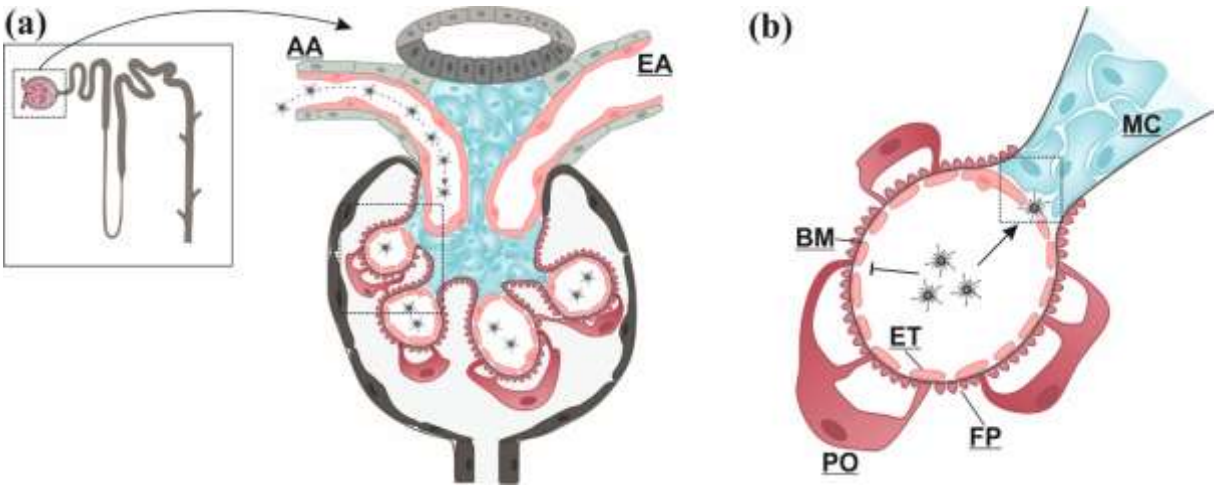

Figure S1. Mesangial accumulation of adenovirus-mimetic NPs. **(a)** Upon i.v. administration, NPs rapidly enter glomerular areas of the kidney via the afferent arteriole that then diverges into the glomerular capillary system.[1] **(b)** Within the capillaries, particles larger than approximately 10 nm cannot pass the renal filter due to its multilayer structure.[2–4] Interstitial mesangial cells, on the contrary, are easily accessible via extravasation through the fenestrated endothelium.[5,6] Having accumulated in mesangial areas, NPs can then finalize cell uptake by mimicking previously described adenoviral cell infiltration (Figure 1). (AA: afferent arteriole; EA: efferent arteriole; MC: mesangial cells; PO: podocyte; FP: foot processes; ET: endothelium; BM: basement membrane

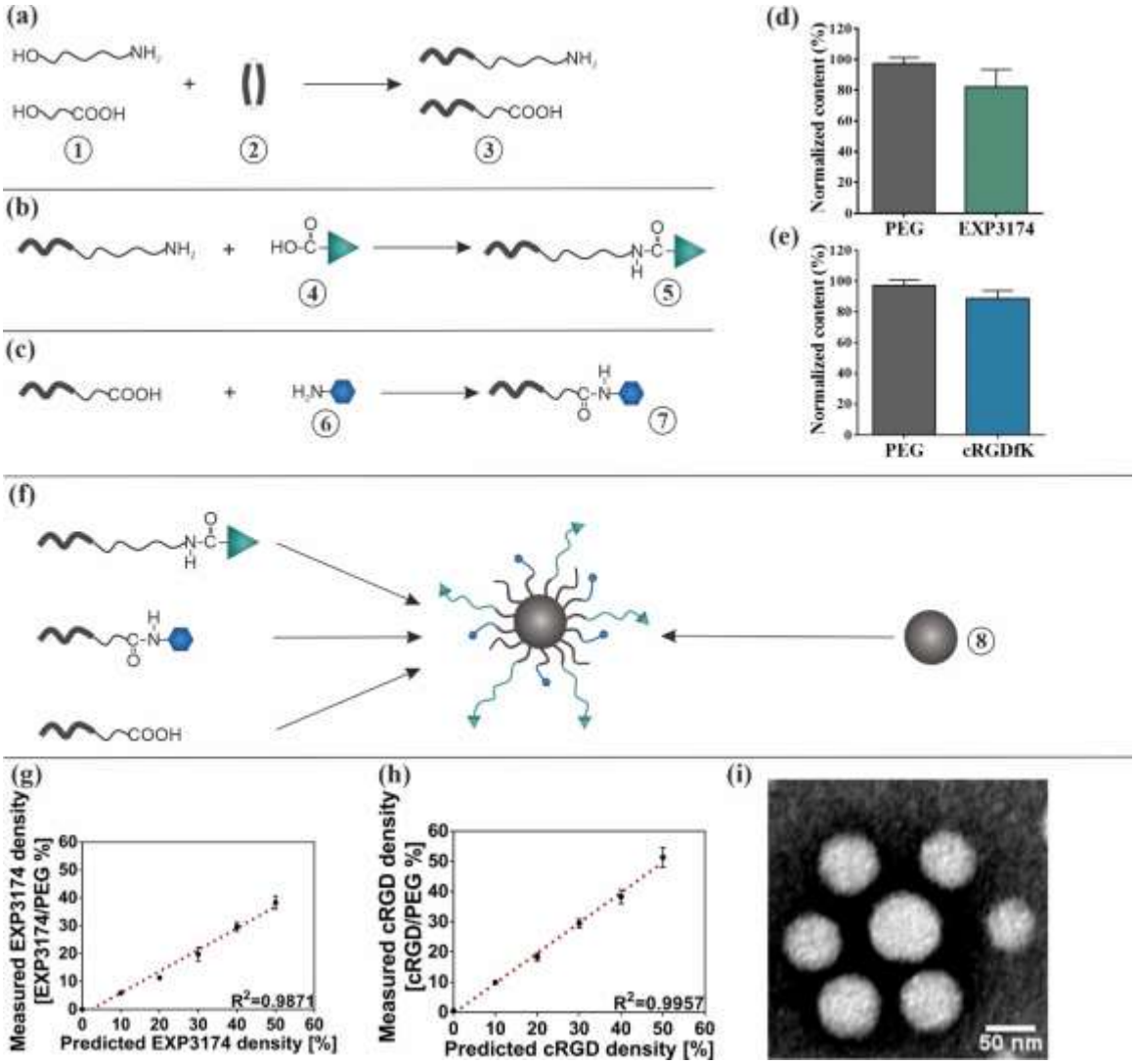

Figure S2. Synthesis concept for ligand-functionalized PEG-PLA block co-polymers. **(a)** Hetero-bifunctional PEG polymers (①) of varying chain length (2 kDa/5 kDa) were mixed with 3,6-dimethyl-1,4-dioxane-2,5-dione (②) to synthesize NH_2-PEG_{5k}-PLA_{10k} as well as COOH-PEG_{2k}-PLA_{10k} (③) via ring-opening polymerization using 1,8-diazabicyclo [5.4.0]undec-7-ene as a catalyst (please refer to the experimental section for a detailed description of the synthesis procedure). **(b)** Subsequently, NH_2-PEG_{5k}-PLA_{10k} was covalently coupled to the carboxyl group of EXP3174 (④) via DCC/NHS chemistry, resulting in EXP3174-PEG_{5k}-PLA_{10k} (⑤). **(c)** Additionally, COOH-PEG_{2k}-PLA_{10k} was attached to the lysine residue of cRGDfK (⑥) via EDC/NHS chemistry, leading to shorter cRGDfK-PEG_{2k}-PLA_{10k} (⑦). **(d)** Coupling efficiency for synthesized EXP3174-PEG_{5k}-PLA_{10k} and **(e)** cRGDfK-PEG_{2k}-PLA_{10k} was determined by independently measuring the concentration of both PEG and EXP3174. Molar concentration thereby did not significantly vary, indicating successful polymer functionalization. **(f)** EXP3174- and cRGDfK-functionalized PEG-PLA polymers were subsequently mixed with unfunctionalized COOH-PEG_{2k}-PLA_{10k} as well as PLGA (⑧) to manufacture hetero-multivalent EXPcRGD NPs. Quantification of EXP3174 **(g)** and **(h)** cRGDfK ligand surface density, respectively, after NP manufacture. Final surface content was directly proportional to the priorly added amount of ligand-functionalized polymer for both EXP3174 (R^2 = 0.9871) and cRGDfK (R^2 = 0.9957), thereby proving sufficient stability of ligand coupling to the respective polymers. **(i)** TEM imaging of EXPcRGD NPs (63,000x magnification). Results represent mean ± SD (n = 3).

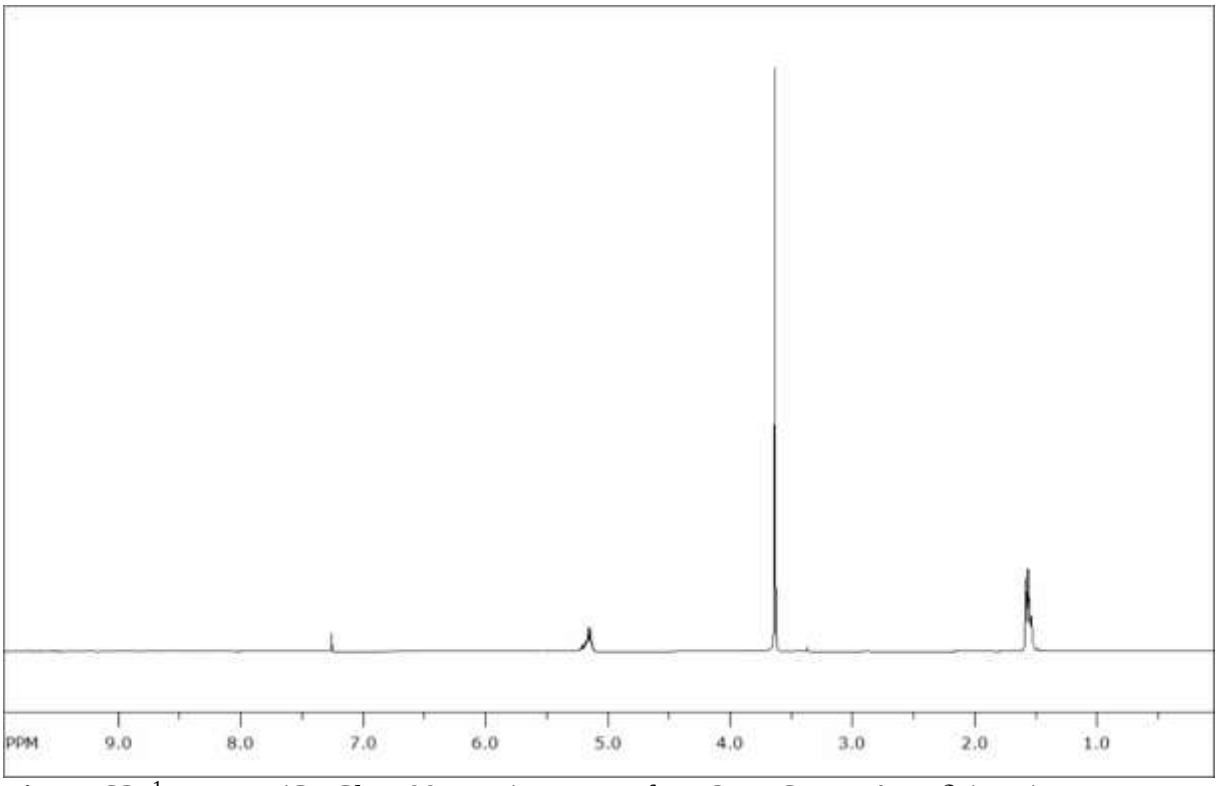

Figure S3. ^{1}H-NMR ($CDCl_3$, 400 MHz) spectra of MeO-PEG_{5k}-PLA_{10k}. δ (ppm): 1.56 ppm (-C(CH_3)H-), 3.37 ppm ($H_3COCH_2CH_2$-), 3.63 ppm (-OCH_2CH_2-), 4.16 (-OCH_2CH_2-O(CO)-), 5.15 ppm (-C(CH_3)H-), 7.26 (solvent peak).

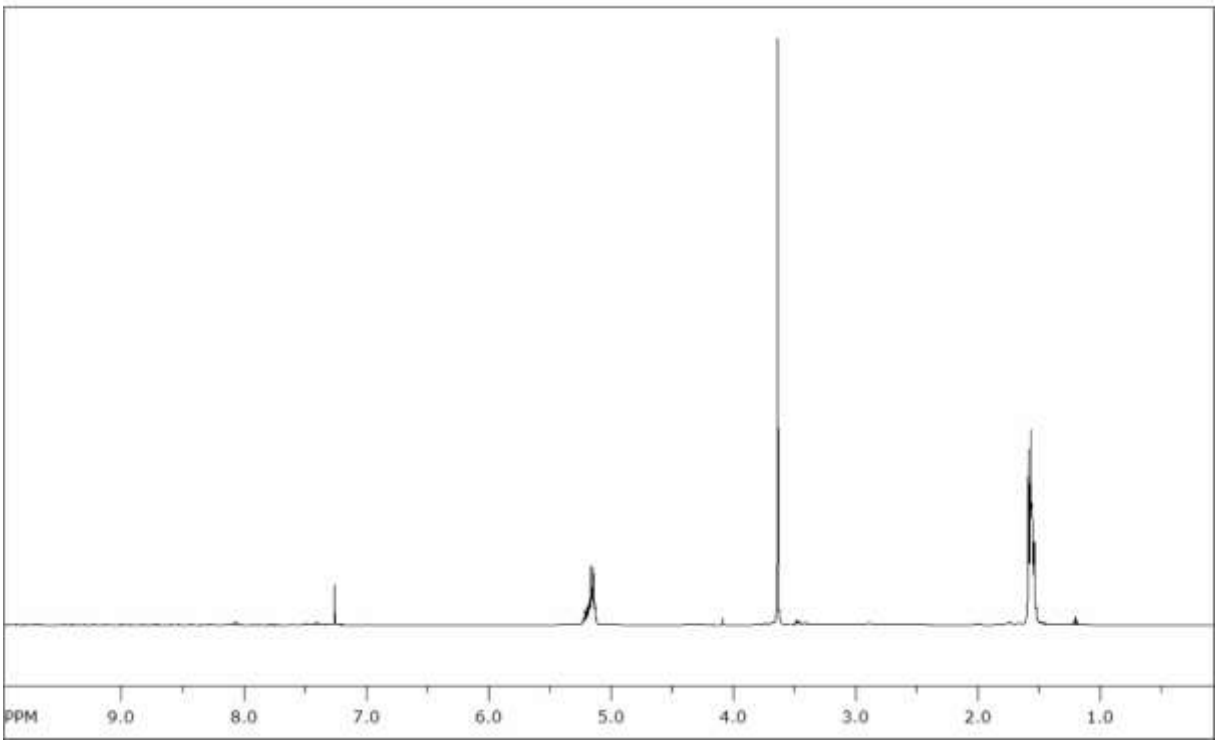

Figure S4. ^{1}H-NMR ($CDCl_3$, 400 MHz) spectra of COOH-PEG_{2k}-PLA_{10k}. δ (ppm): 1.56 ppm (-C(CH_3)H-), 3.40 ppm ($H_3COCH_2CH_2$-), 3.63 ppm (-OCH_2CH_2-), 4.13 (-OCH_2CH_2-O(CO)-), 5.17 ppm (-C(CH_3)H-), 7.26 (solvent peak).

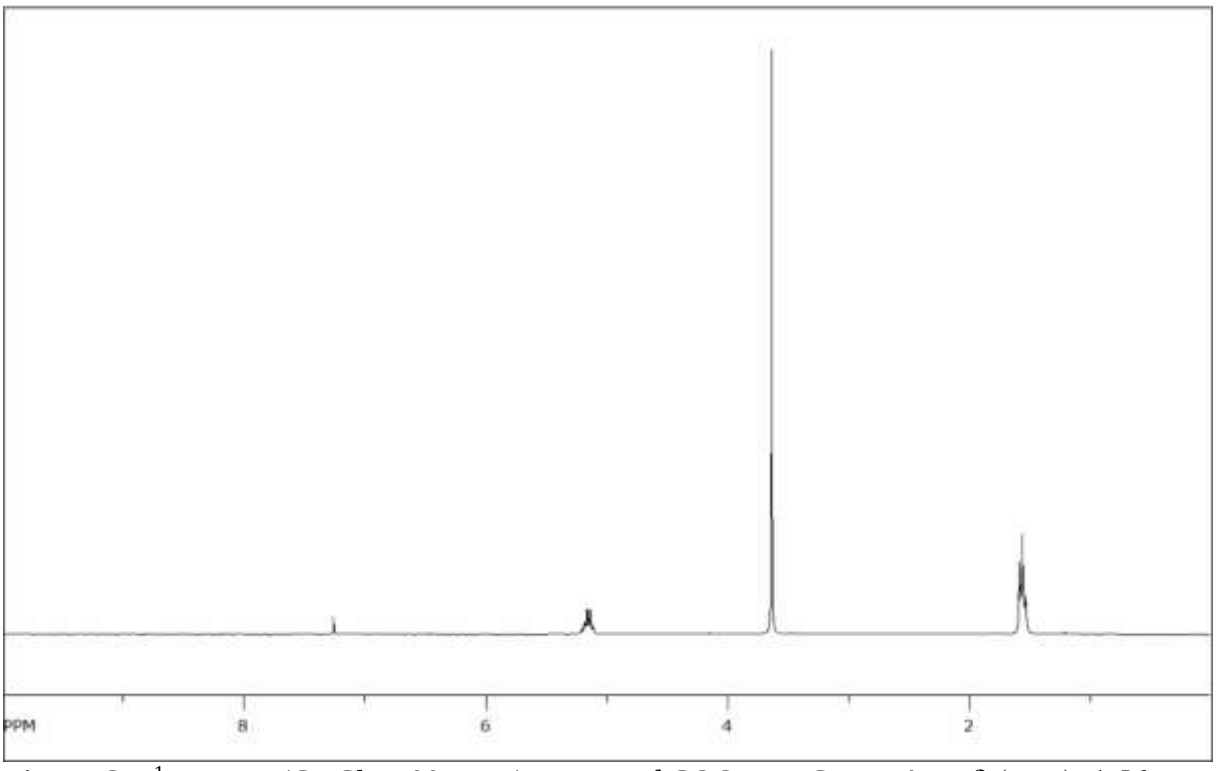

Figure S5. ^{1}H-NMR ($CDCl_3$, 400 MHz) spectra of COOH-PEG_{5k}-PLA_{10k}. δ (ppm): 1.56 ppm (-$C(CH_3)$H-), 3.43 ppm ($H_3COCH_2CH_2$-), 3.63 ppm (-OCH_2CH_2-), 4.15 (-OCH_2CH_2-O(CO)-), 5.16 ppm (-$C(CH_3)$H-), 7.26 (solvent peak).

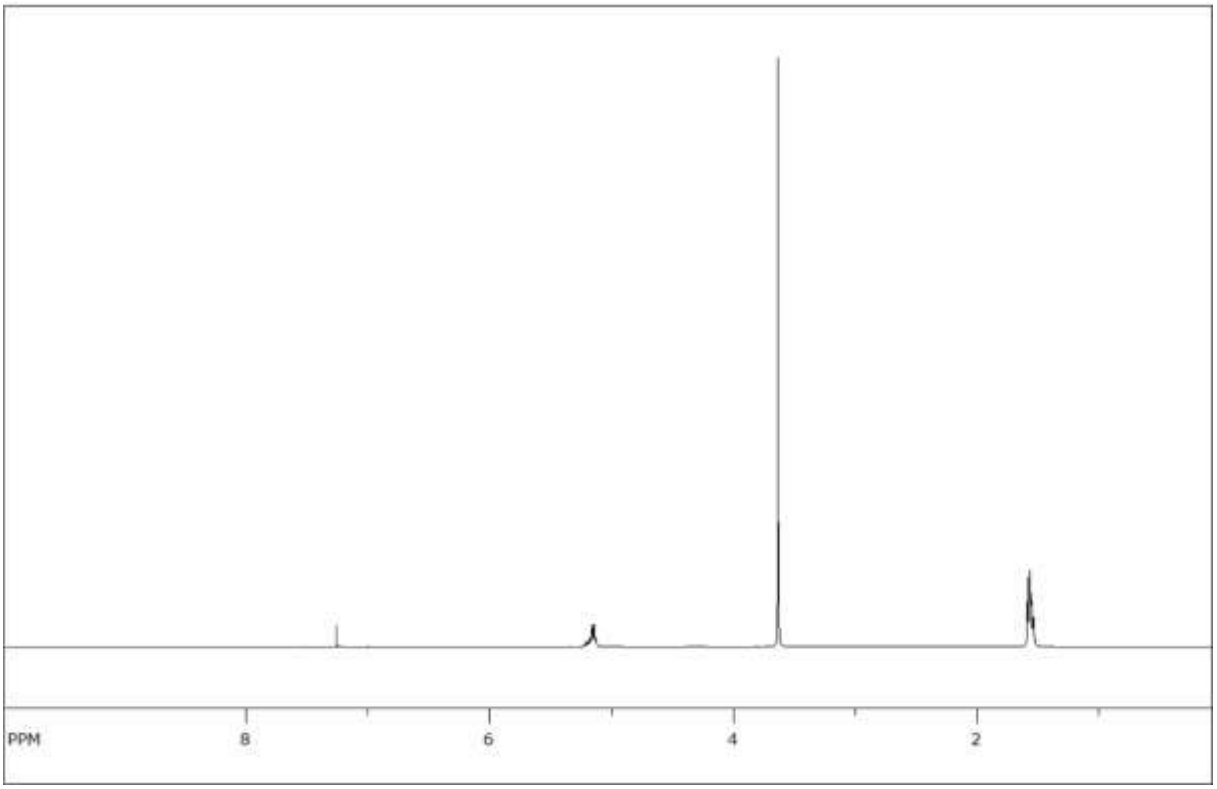

Figure S6. ^{1}H-NMR ($CDCl_3$, 400 MHz) spectra of NH_2-PEG_{5k}-PLA_{10k}. δ (ppm):
1.57 ppm (-$C(CH_3)$H-), 3.39 ppm ($H_3COCH_2CH_2$-), 3.61 ppm (-OCH_2CH_2-), 4.19 (-OCH_2CH_2-O(CO)-), 5.18 ppm (-$C(CH_3)$H-), 7.25 ppm (solvent peak).

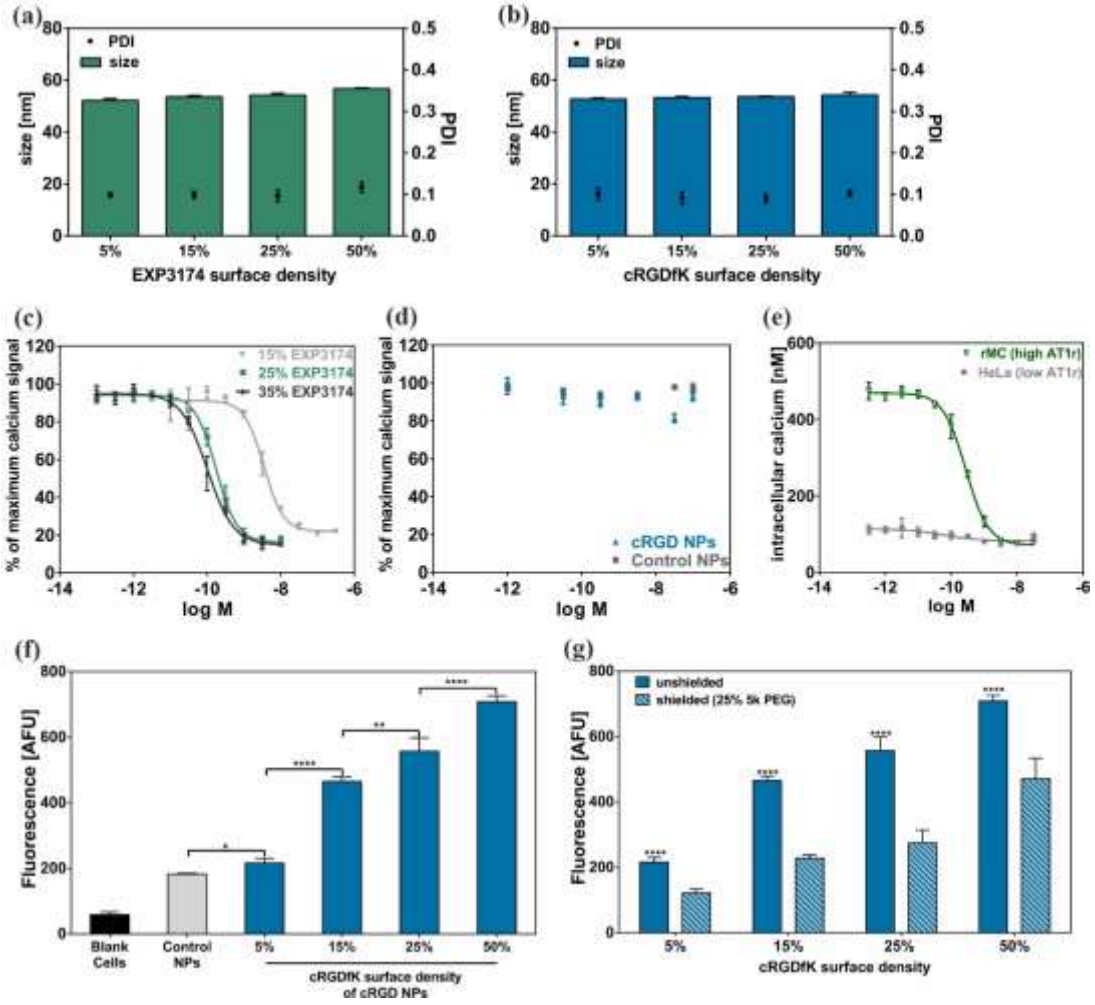

Figure S7. DLS analysis of **(a)** EXP3174-functionalized and **(b)** cRGDfK-functionalized showed no significant impact of the ligand density on the NPs´ hydrodynamic diameter or a possible tendency for aggregation. (PDI: polydispersity index.) **(c)** AT1r activity for rMCs treated with EXP NPs with varying EXP3174 surface densities. EXP NPs with 25 % and 35 % EXP3174 density showed a comparable AT1r blocking **(IC_{50} (25%) = 552 ± 73 pM**; **IC_{50} (35%) = 321 ± 81 pM**), while a surface density of 15 % lead to a drastically reduced AT1r binding (**IC_{50} (15%) = 11 ± 1 nM**). (M = molar NP concentration.) **(d)** AT1r activity for EXP3174-free NPs. Neither unfunctionalized Control NPs nor cRGD NPs could significantly bind the AT1r, resulting in maximum calcium levels upon ATII stimulation and confirming the specificity of the assay. **(e)** Intracellular Ca^{2+} levels for either rMCs (high AT1r expression) or HeLa cells (low AT1r expression)[7] upon incubation with EXPcRGD NPs and stimulation with AT II. Measured intracellular Ca^{2+} levels in HeLa cells were far lower compared to rMCs due to the differences in AT1r expression. (M = molar NP concentration.) **(f)/(g)** Flow cytometry analysis of rMC uptake for cRGDfK-carrying NPs. **(f)** Cell uptake gradually increased with higher surface densities of cRGDfK, as described before.[8] While cRGD NPs with a ligand density of 15% still showed sufficiently enhanced levels of endocytosis, 5% cRGD NPs provided merely low internalization levels, comparable to unfunctionalized Control NPs. **(g)** By introduction of longer shielding elements (see Figure S8), respective rMC uptake could be significantly reduced for all cRGDfK ligand densities. * $P < 0.05$, ** $P < 0.01$, **** $P < 0.0001$. (AFU, arbitrary fluorescence units.) Results represent mean ± SD ($n = 3$).

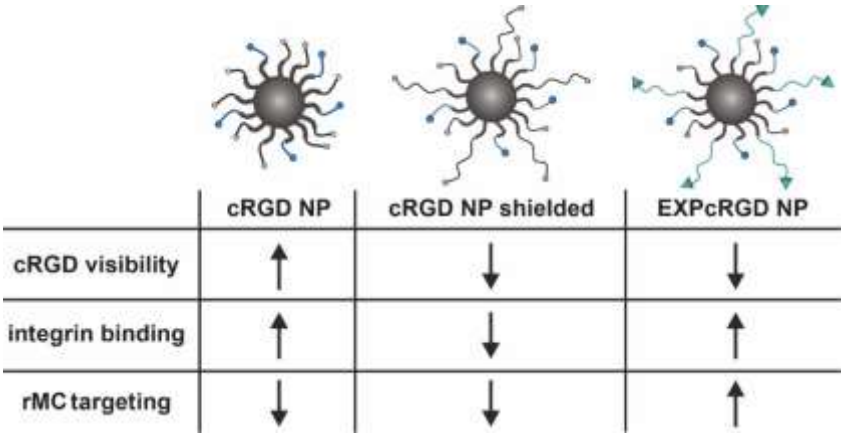

Figure S8. Shielding concept for cRGDfK. While ligand visibility of unshielded cRGD NPs was maximum, introduction of longer COOH-PEG_{5k}-PLA_{10k} chains significantly reduced the accessibility of the ligand due to a steric hindrance effect, leading to a decreased integrin binding and subsequent rMC uptake of shielded cRGD NPs. For EXPcRGD NPs, coupling of EXP3174 to longer PEG_{5k}-PLA_{10k} chains provided the necessary initial binding to the rMC surface. Resulting spatial approach of the NP then lead to a sufficient integrin binding via previously hidden cRGDfK, thereby combining cell-specific targeting and satisfactory uptake.

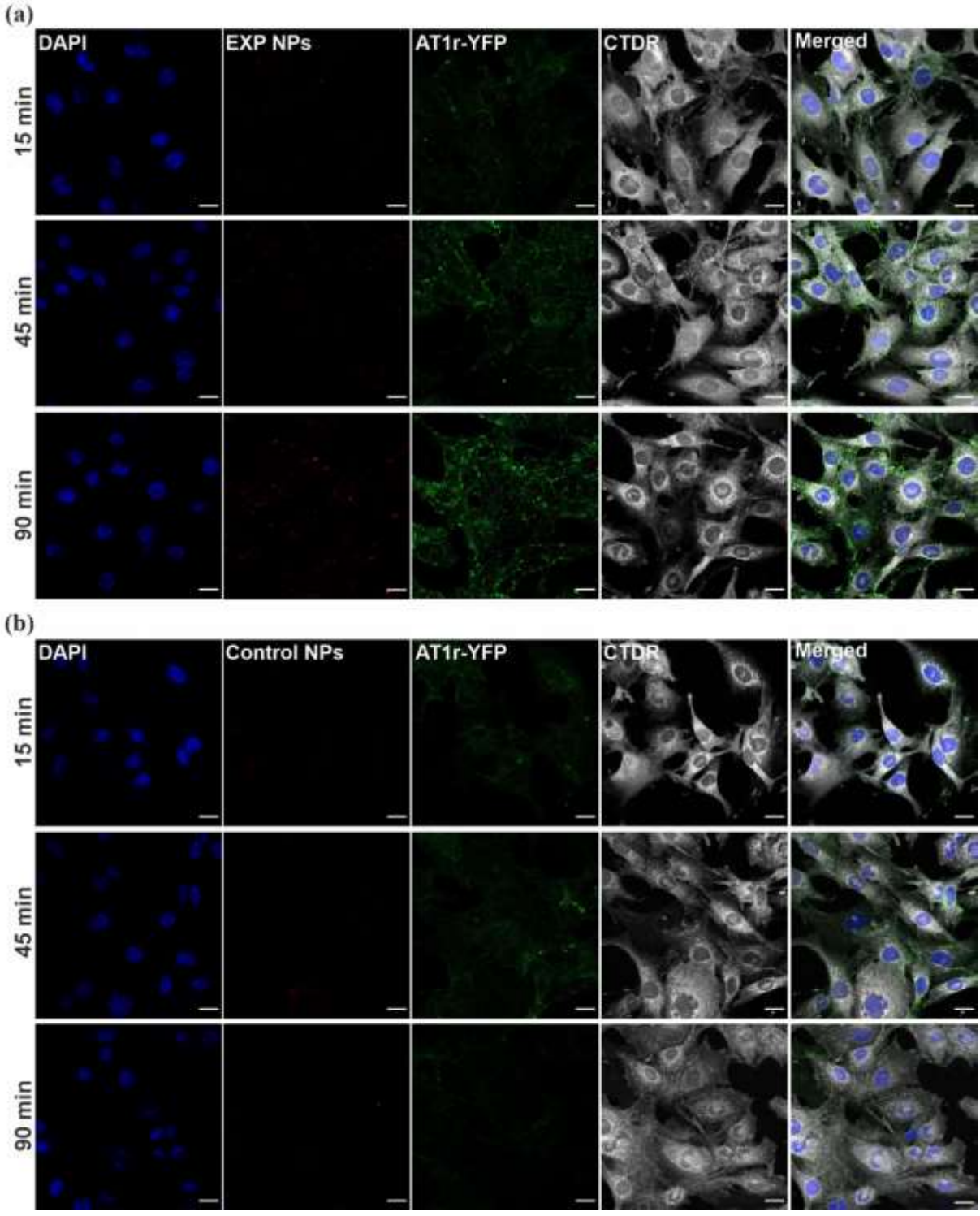

Figure S9. Time-dependent CLSM analysis of NP interaction with AT1r-YFP rMCs (grey). **(a)** For EXP NPs, AT1r signal (green) could mainly be found on the cellular surface, where large receptor clusters became visible and were colocalized with NP-associated fluorescence (red). This indicates EXP NP binding to the AT1r, however without any significant endocytosis. **(b)** Control NPs showed merely negligible levels of rMC uptake. Fluorescence levels for the AT1r were also drastically reduced, as the receptors did not merge to larger formations and remained widely spread across the entire cell surface. (Scale bar 20 µm.)

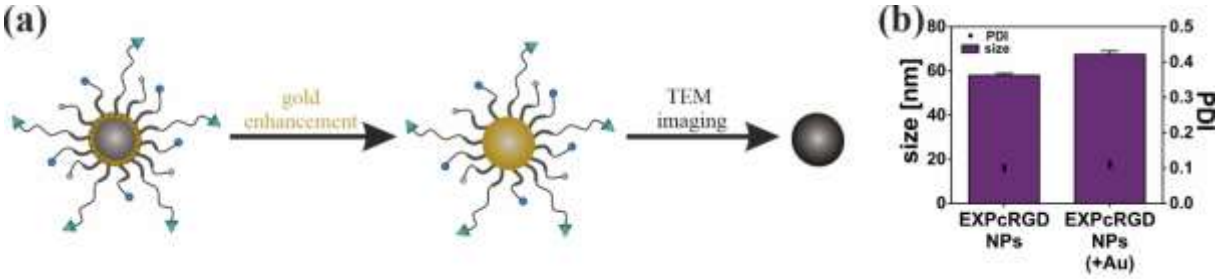

Figure S10. Gold-tagged NPs for facilitated TEM visualization. **(a)** NPs were gold-labeled by covalently attaching ultra-small gold NPs (diameter: 2.2 nm) to the carboxyl group of PLGA, prior to NP manufacturing. After incubation of rMCs with labeled NPs, the particle core was gold-enhanced by depositing further gold particles on the NP core, thereby increasing electron density of the sample and enabling visualization in TEM microscopy, where NPs appeared as dark black spots. **(b)** DLS analysis of NPs. Due to the encapsulation of gold NPs, Au-labeled EXPcRGD NPs showed a slightly increased hydrodynamic diameter with a PDI in a still acceptable range. Results represent mean ± SD (n = 3).

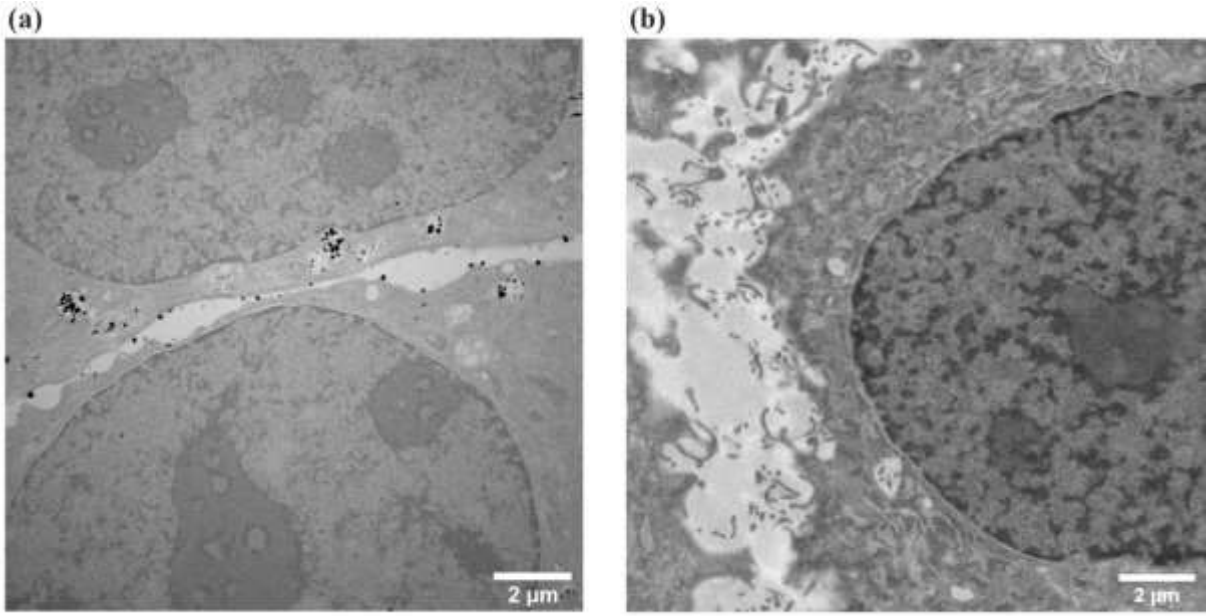

Figure S11. (a) TEM image of rMCs incubated with cRGD NPs. Comparable to EXPcRGD NPs, cRGD NPs showed significant accumulation in endocytotic vesicles within the rMC cytosol. However, NP density on the cellular surface appeared to be lower, indicating that NPs were already taken up to a large degree via integrin-mediated endocytosis. **(b)** TEM image of untreated rMCs after gold-enhancement. Control cells were treated with the same TEM preparation protocol, however without NP incubation. Consequently, no gold deposition was visible, indicating that the applied gold-enhancement did not lead to unspecific staining.

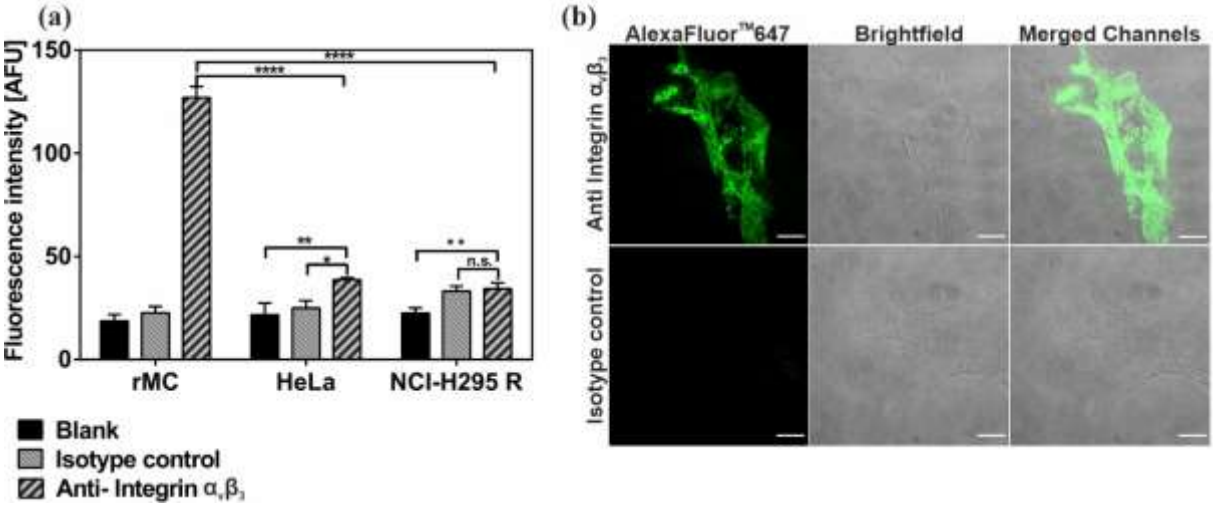

Figure S12. $\alpha_v\beta_3$ expression by different cell types investigated by **(a)** flow cytometry and (**b**) CLSM. For cytometry analysis, unspecific binding sites were blocked with 2% BSA in DPBS and 10^5 cells were incubated for 1 h with a 1:20 dilution of AlexaFluor® anti - CD51/61 antibody in 0.1% BSA in DPBS (AlexaFluor® Mouse IgG1, κ Isotype Ctrl (FC) served as unspecific control). Thereafter, cells underwent several steps of DPBS washing and centrifugation. Finally, samples were resuspended in DPBS and analyzed using flow cytometry as previously described (FACS Calibur, excitation: 633 nm, emission: 661/16 nm bandpass filter). $\alpha_v\beta_3$-derived fluorescence levels were thereby highest for rMCs. While NCI-H295R cells showed no significant integrin expression, HeLa cells were found to have a rather low integrin density, which, however, was still significantly greater than for the isotype control. Results represent mean ± SD (n=3).****P < 0.0001, **P < 0.01, *P < 0.05. (AFU, arbitrary fluorescence units.) For visualization and confirmation of flow cytometry results, rMCs were seeded into 8-well Ibidi slides (15.000 cells well^{-1}) and stained for $\alpha_v\beta_3$ integrin as described above. Cells were then washed with DPBS, fixed with 4% PFA in DPBS and analyzed at a Zeiss LSM 710. CLSM images revealed a strong integrin signal that was co-localized with rMC cell body, indicating a substantial $\alpha_v\beta_3$ receptor density on the surface of mesangial cells. Scale bar = 20 µm.

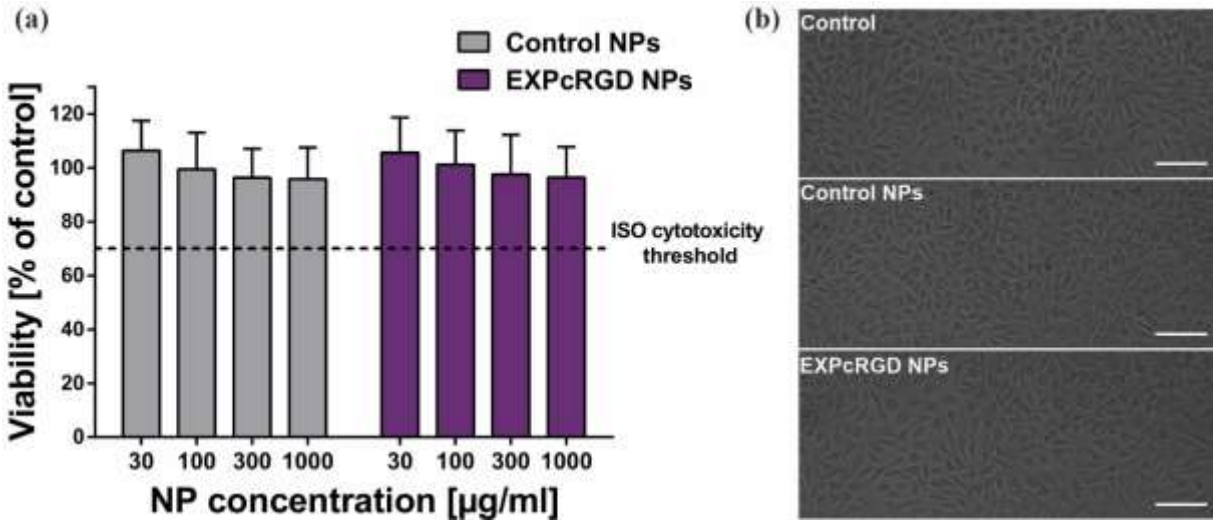

Figure S13. L-929 cell viability after 24 h of incubation with Control and EXPcRGD NPs. **(a)** Cytotoxicity of unfunctionalized and ligand-carrying NPs was tested as described before[9], using a 3-(4,5-dimethylthiazol-2-yl)-2,5-diphenyltetrazolium bromide (MTT) reduction assay according to ISO 10993 – 5:2009 (Biological evaluation of medical devices, part 5: Tests for in vitro cytotoxicity). In brief, mouse fibroblast L-929 cells were seeded at a density of 10,000 cells per well and incubated for 24 h (37 °C / 5 % CO_2). NPs were manufactured in mpH_2O under aseptic conditions. To further decrease microbial contamination, NPs were exposed to UV-light for 3 h. Samples were thereafter adjusted to concentrations from 30 to 1000 µg mL^{-1} in EMEM medium containing 10 % FCS and incubated with cells for 24 h. (Positive control: 0.1 % SDS; negative control: pure medium.) Thereafter, samples were removed and 50 µL EMEM medium containing 1.0 mg mL-1 MTT were added. After 2 h of incubation, the MTT solution was aspirated and 100 µL isopropanol was added to each well. After 30 min of incubation under gentle shaking and light exclusion, absorbance at 570 and 690 nm was measured using a FluoStar Omega fluorescence microplate reader (BMG Labtech, Ortenberg, Germany). Viability was assessed using the difference in absorbance at 570 and 690 nm and normalized to the negative control. Results represent mean ± SD (n = 6). **(b)** Brightfield images of L-929 cells incubated with either no NPs or 1000 µg mL^{-1} of Control/EXPcRGD NPs. (Scale bar 100 µm.)

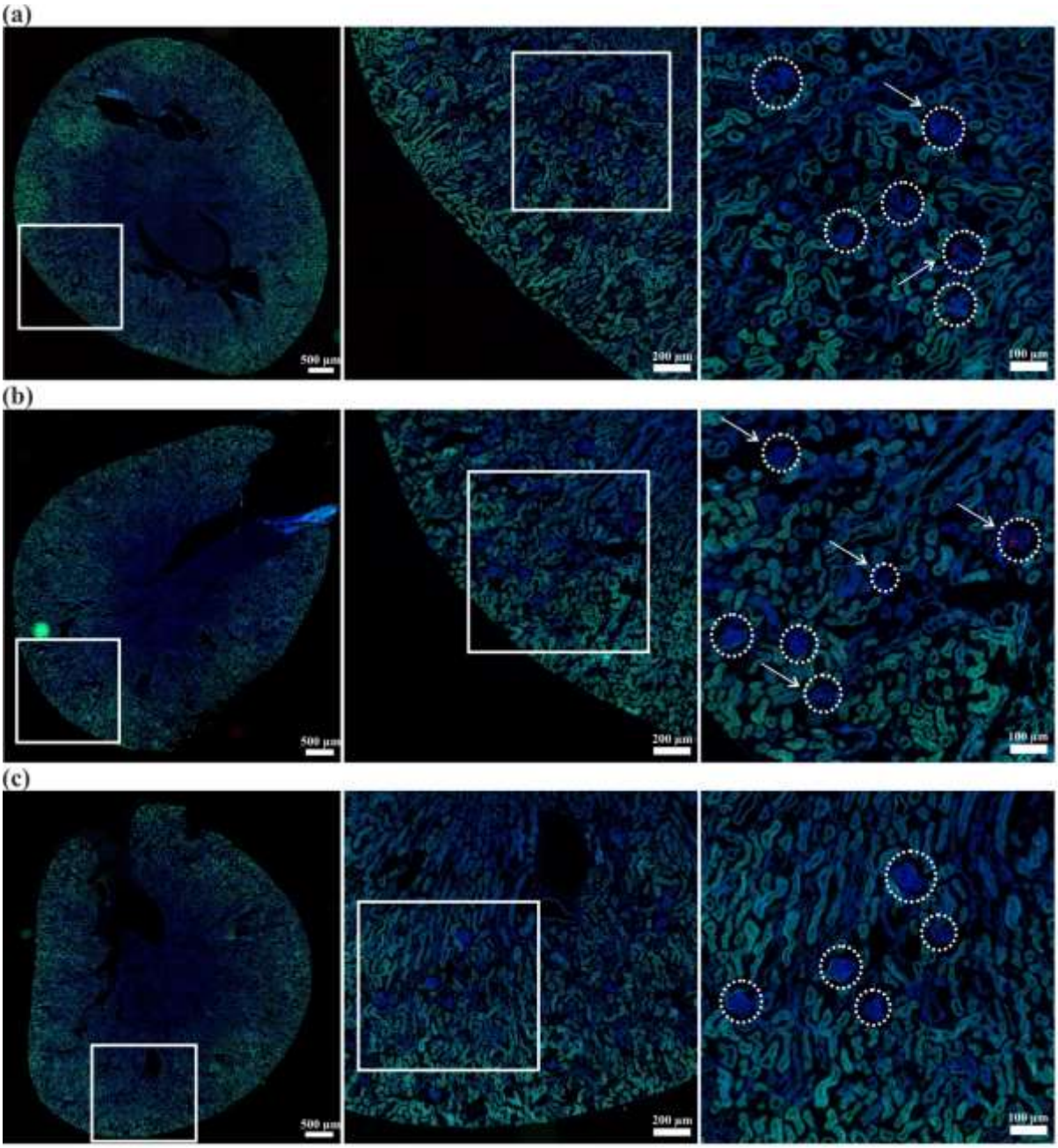

Figure S14. Fluorescence analysis of kidney cryosections. Cell nuclei were stained with DAPI (blue). Additionally, kidney autofluorescence (green) was recorded to facilitate histological evaluation of samples. NP-derived fluorescence is shown in red. **(a)** Unfunctionalized Control NPs showed only weak fluorescence levels in renal glomeruli, while EXP NPs **(b)** accumulated in a considerable amount in glomerular areas (white circles; arrows indicate fluorescence-positive glomeruli.). However, fluorescence intensity was significantly lower than for EXPcRGD NPs (Figure 7). **(c)** For cRGD NPs, fluorescence signal was minimal with no visible particle accumulation in any glomerulus. For all depicted NP species, tubular fluorescence was negligible, indicating that no renal filtration had taken place. (Images on the right show magnified sections of white boxes indicated in the respective left images.)

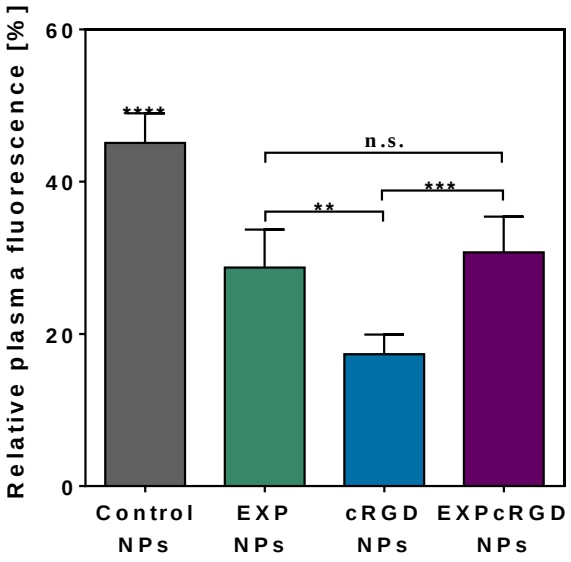

Figure S15. Relative blood plasma fluorescence after NP injection. Control NPs exhibited the highest blood circulation values with almost 50% residual blood plasma fluorescence after 60 min of injection compared to the value after 5 min. In contrast to EXP NPs as well as EXPcRGD NPs, that both showed tolerable residual concentrations, cRGD NPs were rapidly cleared from the blood. Results represent mean ± SD (*n*=3). ****P < 0.0001, ***P < 0.001, **P < 0.01. (n.s.: not significant.)

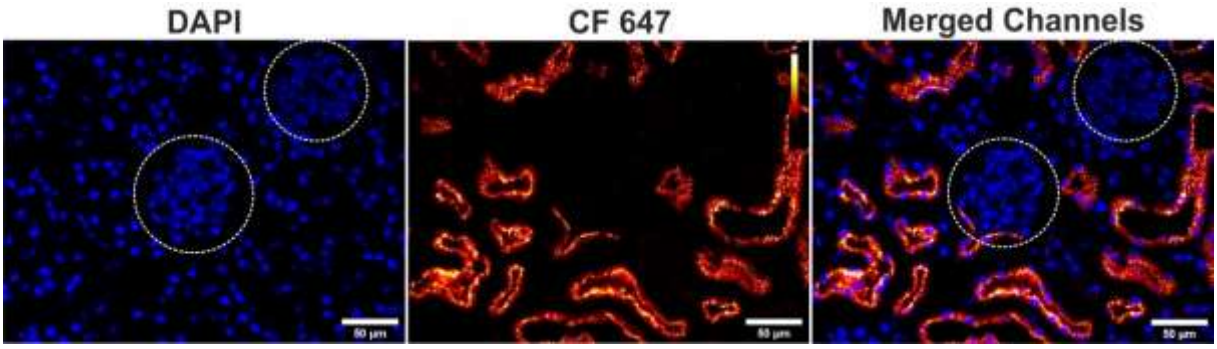

Figure S16. Fluorescence imaging of kidney cryosections after injection of free CF^{TM} 647 fluorescent dye. To visualize cell nuclei, sections were DAPI-stained (blue). After injection of a comparable molarity of free dye, strong fluorescence signals (red to white) could be detected in tubular areas of the kidney, indicating free renal filtration of the low-molecular dye. As expected, no intraglomerular accumulation could be detected (white circles). (Calibration bar: 0 - 65535 Gray Value.)

References

(1) Scott, R. P.; Quaggin, S. E. The Cell Biology of Renal Filtration. *J. Cell Biol.* **2015**, *209*, 199–210.

(2) Miner, J. H. The Glomerular Basement Membrane. *Exp. Cell Res.* **2012**, *318*, 973–978.

(3) Haraldsson, B.; Nyström, J.; Deen, W. M. Properties of the Glomerular Barrier and Mechanisms of Proteinuria. *Physiol. Rev.* **2008**, *88*, 451–487.

(4) Choi, H. S.; Liu, W.; Misra, P.; Tanaka, E.; Zimmer, J. P.; Itty Ipe, B.; Bawendi, M. G.; Frangioni, J. V. Renal Clearance of Quantum Dots. *Nat. Biotechnol.* **2007**, *25*, 1165–1170.

(5) H. Latta. An Approach to the Structure and Function of the Glomerular Mesangium. *J. Am. Soc. Nephrol.* **1992**, *2*, 65–73.

(6) Satchell, S. C.; Braet, F. Glomerular Endothelial Cell Fenestrations: an Integral Component of the Glomerular Filtration Barrier. *Am. J. Physiol. Renal Physiol.* **2009**, *296*, 947-956.

(7) Hennig, R.; Ohlmann, A.; Staffel, J.; Pollinger, K.; Haunberger, A.; Breunig, M.; Schweda, F.; Tamm, E. R.; Goepferich, A. Multivalent Nanoparticles Bind the Retinal and Choroidal Vasculature. *Journal of controlled release : official journal of the Controlled Release Society* **2015**, *220*, 265–274.

(8) Abstiens, K.; Gregoritza, M.; Goepferich, A. M. Ligand Density and Linker Length are Critical Factors for Multivalent Nanoparticle-Receptor Interactions. *ACS Appl. Mater. Interfaces* **2019**, *11*, 1311–1320.

(9) Abstiens, K.; Fleischmann, D.; Gregoritza, M.; Goepferich, A. M. Gold-Tagged Polymeric Nanoparticles with Spatially Controlled Composition for Enhanced Detectability in Biological Environments. *ACS Appl. Nano Mater.* **2019**, *2*, 917–926.